Supplementary material of "All-optical spatiotemporal oscilloscope for few-cycle optical waveform"

In this supplementary material, we provide important information to support the feasibility of our work. Section 1 presents the derivation of the equations in the manuscript. Section 2 presents the simulations of the high harmonic spectrum. Section 3 provides the reconstruction results of the electric field with different effects and different order dispersions. Section 4 shows a comparison of the delay and spatial dependent frequency shift of the 33^{rd}-order harmonic in near and far fields. Section 5 presents the result of FROG measurement. Section 6 presents the simulation of the reconstruction under various CEP conditions. Section 7 shows the limitation tests of the approach. Section 8 presents the simulation of the reconstruction with different wavelengths of the perturbing field.

Section 1: Derivation of the equations

Ionization time and radiation time of high harmonic exist in pairs under the saddle point model [32]. When the perturbing field is sufficiently weak, it does not affect the ionization process but mainly perturbs the free electron's trajectory, the time-dependent dipole moment [42] including the spatial coordinate can be approximately written as:

$$d\left(t_e,\tau,x_f\right)=\sum\nolimits_k d_0^k\left(t_e,x_f\right)e^{-i\sigma^k\left(t_e,\tau,x_f\right)}+c.c, \tag{S1}$$

where the subscript k denotes the corresponding quantum trajectory, d_0^k is the dipole without perturbing fields, t_e is the emission time of the high harmonics, τ is the delay between the driving field and the perturbing field, x_f is the space coordinate in the near field, and σ is the perturbing phase. When we introduce the perturbing field to perturb the high harmonic generation process, an additional phase will be introduced, which can be written as:

$$\sigma^k(t_e,\tau,x_f)=\mathrm{S}_1(t_e,\tau,x_f)-\mathrm{S}_0(t_e,x_f), \tag{S2}$$

where S_1 and S_0 represent the quasiclassical action with and without the perturbing field, respectively.

$$\mathrm{S}_0(t_e,x_f)=\int_{t_i}^{t_e}dt'\left[v(t',x_f)^2/2+I_p\right], \tag{S3}$$

where v is the velocity. Eqn.(S2) can be written as:

$$\begin{aligned}\sigma^k(t_e,\tau,x_f)&=\int_{t_i}^{t_e}\left[\left(v_d+v_p\right)^2/2+I_p\right]dt-\int_{t_i}^{t_e}\left(v_d^2/2+I_p\right)dt\\&\approx-\int_{t_i}^{t_e}\left(v_dA_p\right)dt,\end{aligned} \tag{S4}$$

where A_p is the vector potential of the perturbing field, $v_d(v_p)$ is the velocity of the quantum trajectory under the driving (perturbing) field. According to the approximation in Ref [26], Eqn.(S4) is reduced to:

$$\sigma^k(t_e,\tau,x_f) \approx -\frac{9}{128} e_d \omega_d t_e^4 E_p\left(\tau+\zeta_\varepsilon, x_f\right), \tag{S5}$$

where ω_d and e_d are the frequency and the amplitude of the driving field, E_p is the perturbing field, and ζ_ε is constant.

When the high harmonic radiated from two slits are in a condition of constructive interference, the total phase difference is [24]:

$$\Delta\phi\left(\omega,\tau,x_f\right) = \sigma_2^k\left(t_e,\tau,x_f\right) - \sigma_1^k\left(t_e,\tau,x_f\right) + \omega T_0/2 + \pi + \gamma = 2m\pi, \tag{S6}$$

where T_0 is the optical cycle of the driving field, ω is the frequency of the high harmonics, γ is the non-adiabatic effect constant [33], and m is an integer. Since the electric fields of neighboring time slits are reversed, their perturbing phases are also reversed: $\sigma_1^k\left(t_e,\tau,x_f\right) = -\sigma_2^k\left(t_e,\tau,x_f\right)$. Then the perturbing phase of the first slit and second slit can be respectively written as:

$$\sigma_1^k(t_e,\tau,x_f) = -\frac{9}{128} e_d \omega_d t_e^4 E_p\left(\tau+\zeta_\varepsilon, x_f\right), \tag{S7}$$

$$\sigma_2^k(t_e,\tau,x_f) = \frac{9}{128}\alpha(x_f) e_d \omega_d t_e^4 E_p\left(\tau+\zeta_\varepsilon+\Delta(x_f), x_f\right), \tag{S8}$$

where $\alpha(x_f)$ is the intensity ratio of the driving field between two neighboring slits, $\Delta(x_f)$ is the time difference between the two attosecond time slits. Combining Eqn.(S6), Eqn.(S7), with Eqn.(S8) yields:

$$-9/128 e_d \omega_d t_e^4\left[\alpha(x_f) E_p\left(\tau+\zeta_\varepsilon+\Delta(x_f), x_f\right) + E_p\left(\tau+\zeta_\varepsilon, x_f\right)\right] + \omega T_0/2 + \pi + \gamma = 2m\pi, \tag{S9}$$

$$\omega = (2m-1)\,\omega_d - \frac{2\gamma}{T_0} + \frac{9 e_d \omega_d t_e^4}{64 T_0}\left[\alpha(x_f) E_p\left(\tau+\zeta_\varepsilon+\Delta(x_f), x_f\right) + E_p\left(\tau+\zeta_\varepsilon, x_f\right)\right], \tag{S10}$$

and the frequency shift can be derived as:

$$\delta\omega(t_e,\tau,x_f) = \frac{9 e_d \omega_d t_e^4}{64 T_0}\left[\alpha(x_f) E_p\left(\tau+\zeta_\varepsilon+\Delta(x_f), x_f\right) + E_p\left(\tau+\zeta_\varepsilon, x_f\right)\right]. \tag{S11}$$

Here we are considering the frequency shift of a specific high harmonic order, and once the order is determined, t_e and ζ_ε are also determined:

$$\delta\omega\left(\tau, x_f\right) = \beta(x_f)(\alpha\left(x_f\right) E_p\left(\tau+\Delta(x_f), x_f\right) + E_p\left(\tau, x_f\right)), \tag{S12}$$

where $\beta(x_f)$ is the constant.

Section 2: The simulation of high harmonic spectrum

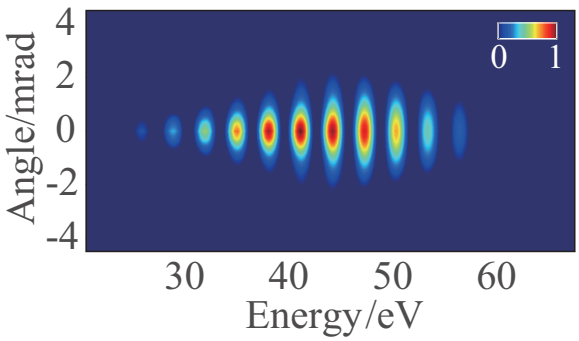

Figure S1: The simulation of high harmonic spectrum in the far field.

Here we add the time window functions (super-Gaussian window $\exp\left[-\left(\frac{\kappa_1 \Delta t}{\kappa_2 T_0}\right)^4\right]$, where κ_1 and κ_2 is adjustment parameters of the functions, Δt is the width of the windows) on the radiation dipole moment of electron. Two short trajectories are selected for high harmonic generation while ignoring the propagation effect and Fig.S1 is the far field high harmonic spectrum after selecting the short trajectories.

Section 3: The simulation reconstruction of the electric fields with different effects and different order dispersions

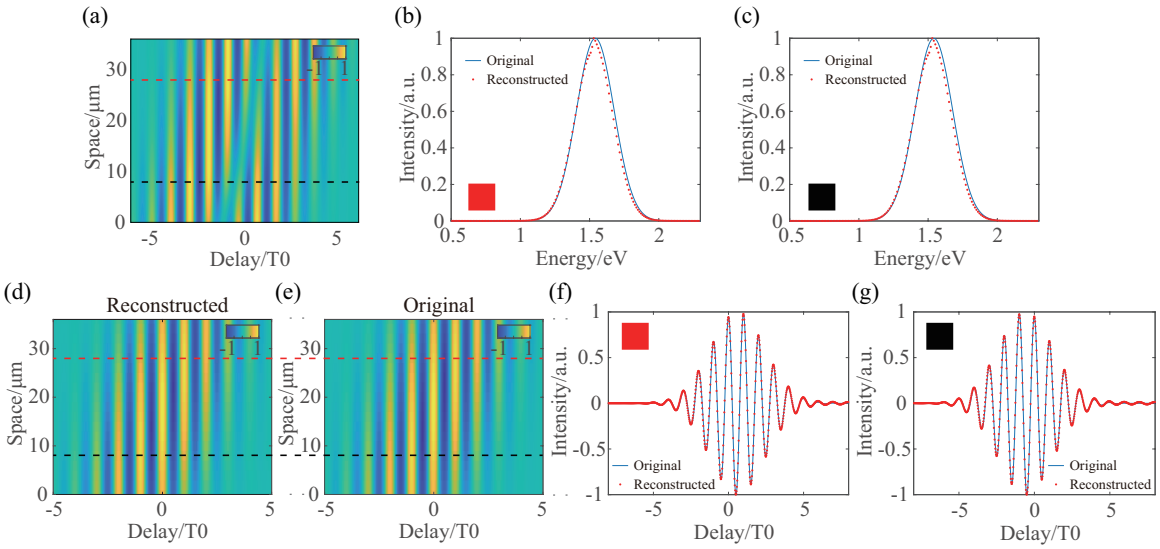

Figure S2: (a) The variation of the center of mass of the 33^{rd}-order harmonic spectrum in near field with delay and space after introducing the perturbing field with pulse front tilt effect. Two spatial positions are selected to compare the reconstruction results, and the selected positions are indicated by the red and black dashed lines, respectively. (b) A comparison of the reconstructed and original spectrum for the position indicated by the red dashed line. (c) is the same as (b) but for the position indicated by the black dashed line. (d) and (e) is the reconstructed and original two-dimensional electric field with pulse front tilt effect, respectively. (f) and (g) show the comparison of the reconstructed and original electric fields at locations indicated by the red and black dashed lines in (a), respectively.

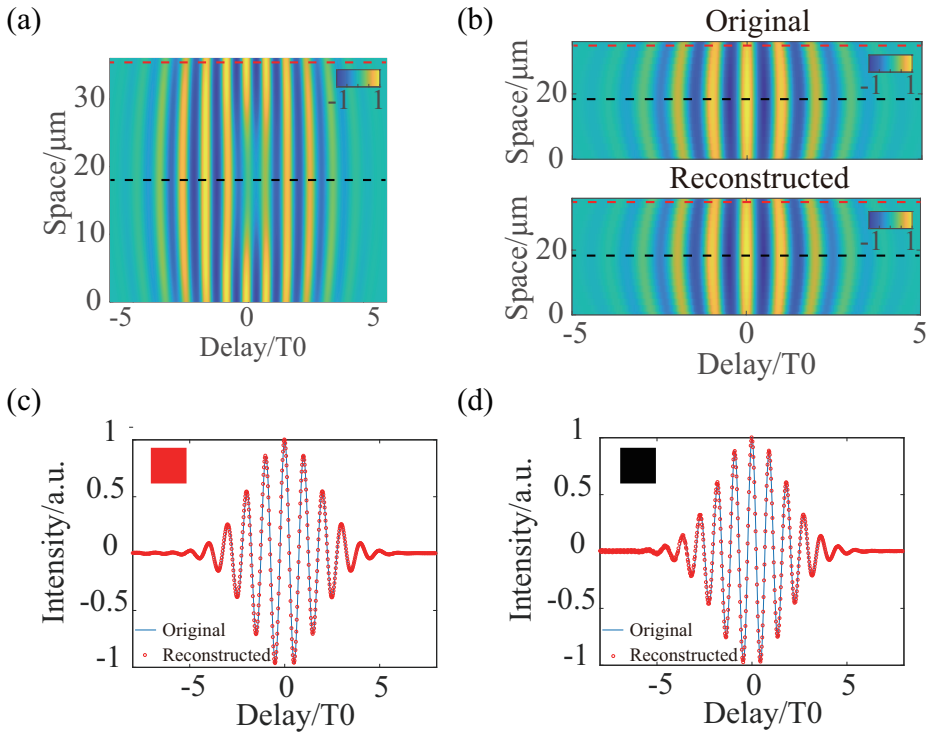

Figure S3: (a) The variation of the center of mass of the 33^{rd}-order harmonic spectrum in near field with delay and space after introducing the perturbing field with second order spatiotemporal coupling effect from the simulation. Two spatial positions are selected to compare the reconstruction results, and the selected positions are indicated by the red and black dashed lines, respectively. (b) The original and reconstructed two-dimensional electric field with second order spatiotemporal coupling effect. (c) and (d) are the comparison of the reconstructed and original electric fields at locations indicated by the red and black dashed lines in (a), respectively.

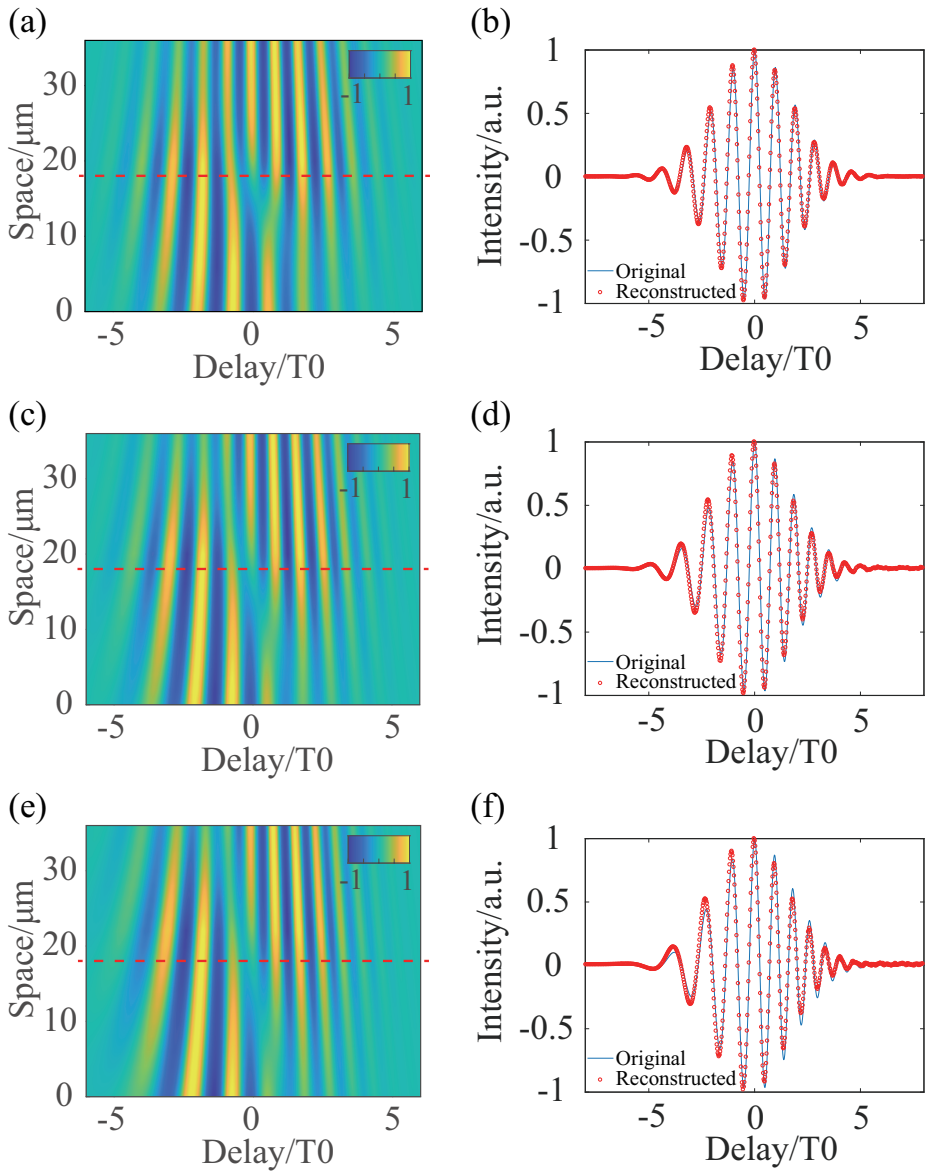

Figure S4: (a) The variation of the center of mass of the 33^{rd}-order harmonic spectrum in near field as a function of delay and space after introducing a temporally and spatially chirped perturbing field: $\mathrm{E}_p\left(t, x_f\right) = e_p \exp\left(-\frac{t^2}{{T_f}^2} - \frac{{x_f}^2}{{w_f}^2}\right) \cos\left(\left(\omega_p + \eta x_f\right) t + \varepsilon t^2\right)$, where $e_p(\omega_p)$ is the amplitude (frequency) of the perturbing field, T_f is the duration, w_f is the spot size, η is the spatial chirp parameter, and ε is the temporal chirp parameter. (a) and (b) ε = 17.3 THz/fs; (c) and (d) ε = 34.6 THz/fs; (e) and (f) ε = 51.9 THz/fs.

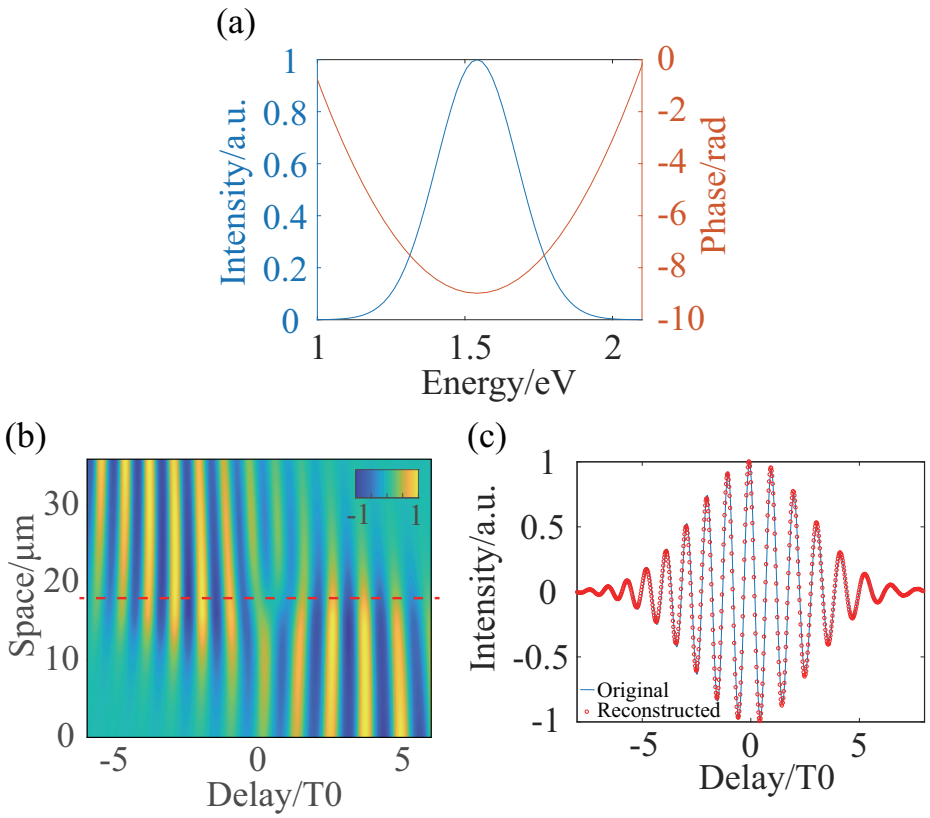

Figure S5: (a) The amplitude and phase of the spectrum of the perturbing field. (b) The variation of the center of mass of the 33^{rd}-order harmonic spectrum in near field as a function of delay and space. (c) The comparison of the reconstructed and original electric fields at locations indicated by the red dashed lines in (b).

The reconstruction result of the electric field with spatial chirp effect and a second-order dispersion of 24 fs^2 is shown in Fig.S5.

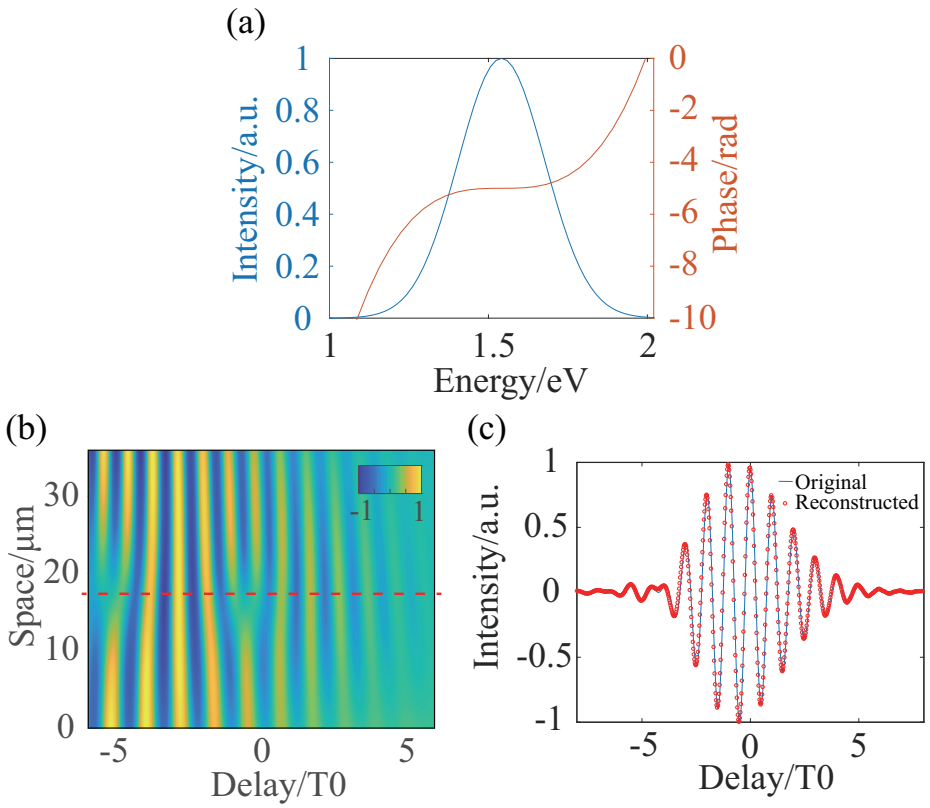

Figure S6: The same as Fig.S5 but for the electric field with the third-order dispersion.

The reconstruction result of the electric field with spatial chirp effect and a third-order dispersion of 90 fs^3 is shown in Fig.S6.

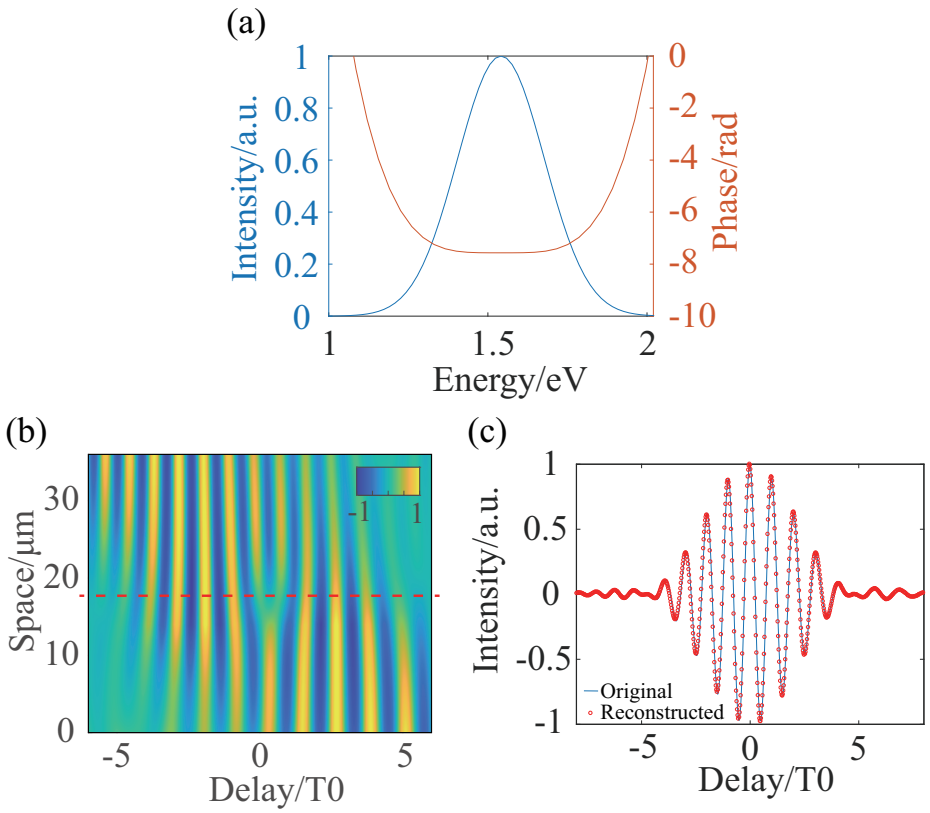

Figure S7: The same as Fig.S5 but for the electric field with the forth-order dispersion.

The reconstruction result of the electric field with spatial chirp effect and a fourth-order dispersion of 720 fs^4 is shown Fig.S7.

Section 4: Comparison of the frequency oscillations of the 33^{rd}-order harmonic in both near and far fields

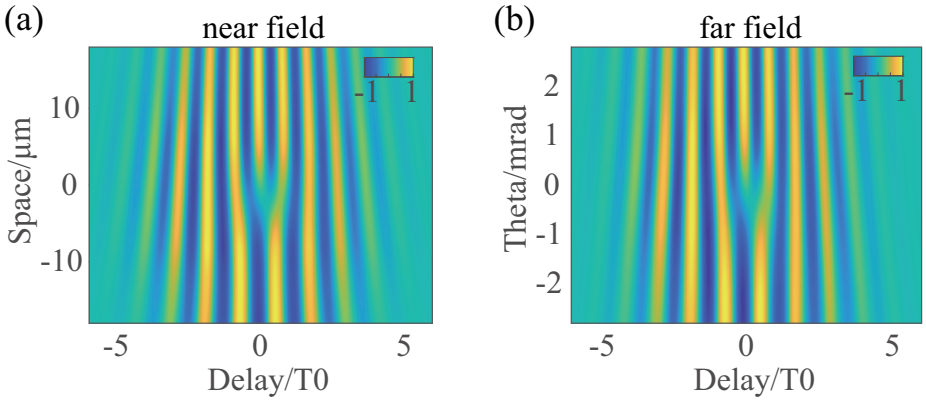

Figure S8: The comparison of the frequency oscillations of the 33^{rd}-order harmonic in both near and far fields.

The simulation results presented in Fig.S8 demonstrate a similarity in the frequency oscillations of a specific high harmonic order in both near and far fields, and both of them can be used to reconstruct the electric field.

Section 5: FROG measurement

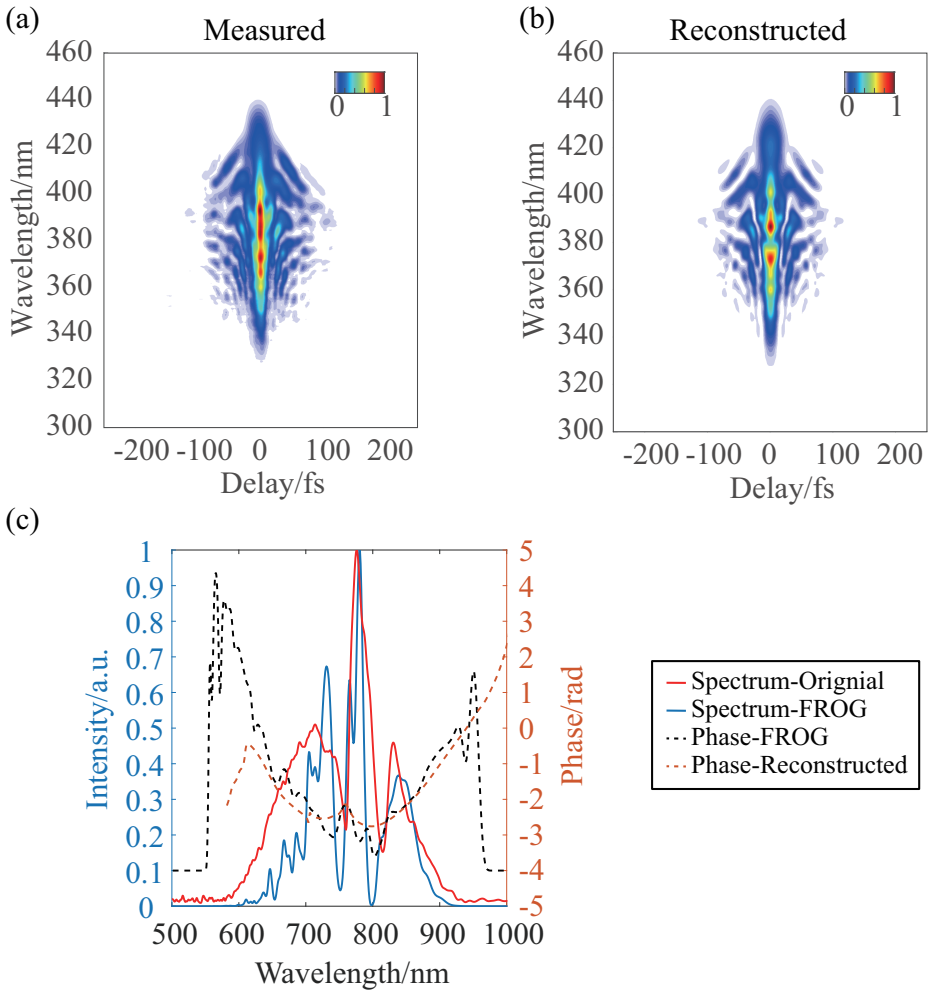

Figure S9: (a) The measured FROG trace. (b) The reconstructed FROG trace. (c) The comparison of the phase and amplitude of the spectrum (the red line is the original spectrum, the blue line is the reconstructed spectrum from FROG, the black dot line is the reconstructed spectral phase from FROG, and the orange dot line is the reconstructed spectral phase from our method).

Section 6: Simulation of the reconstruction under various CEP conditions

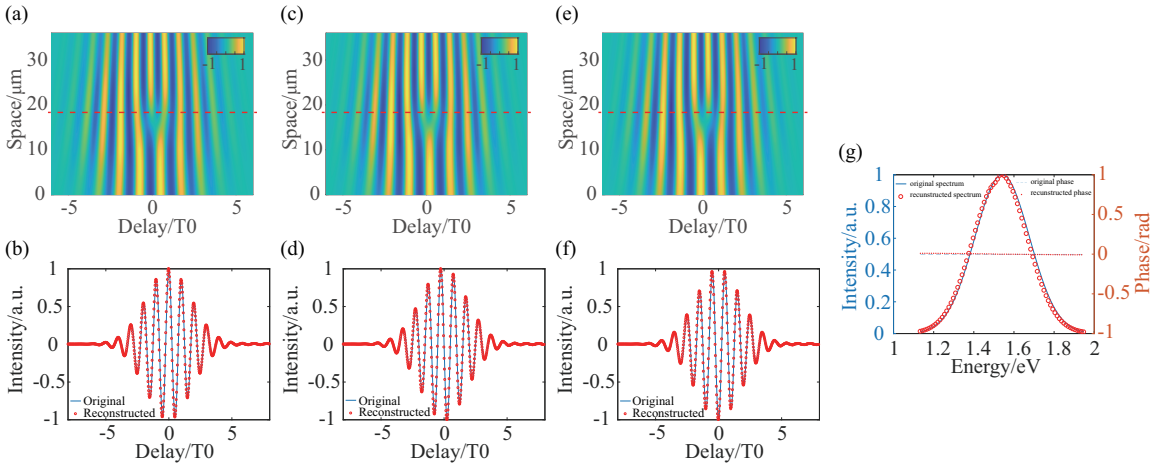

Figure S10: (a) The variation of the center of mass of the 33^{rd}-order harmonic spectrum in near field with delay and space after introducing the perturbing field with spatial chirp effect and CEP condition of 0 from the simulation. (b) The comparison of the reconstructed and original electric fields at locations indicated by the red dashed lines in (a). (c) and (d) The same as (a) and (b) but for the CEP condition of 0.5π. (e) and (f) The same as (a) and (b) but for the CEP condition of π. (g) The comparison of the reconstructed and original spectrum and spectrum phase at locations is indicated by the red dashed lines in (a) (blue line is original spectrum, blue dot line is original spectrum phase, red circle is reconstructed spectrum, red dot is reconstructed spectrum phase).

Section 7: The limitation tests of the approach

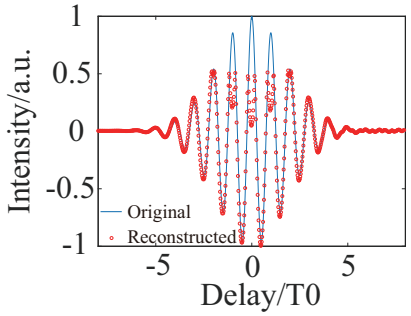

Figure S11: The comparison of the reconstructed and original electric fields after introducing the perturbing field with 10% amplitude ratio

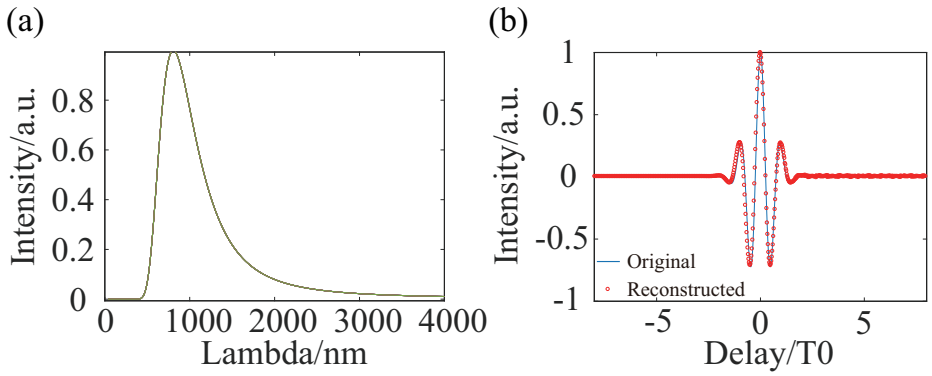

Figure S12: (a) The spectrum of the perturbing field with one cycle pulse duration. (b) The comparison of the reconstructed and original electric fields.

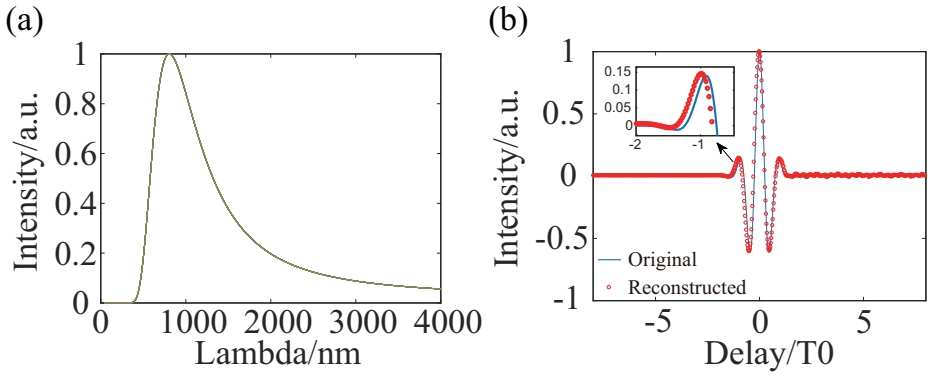

Figure S13: (a) The spectrum of the perturbing field with 0.8 cycle pulse duration. (b) The comparison of the reconstructed and original electric fields.

We have done simulations to test the limitations of our method. Based on the principle, we consider there are two main influences that can cause the method to break down: intensity and spectral bandwidth. Firstly, when the intensity of the perturbing field is too strong, it will not be possible to analyze it using high harmonic perturbation theory. When the amplitude ratio of the perturbation field is 10%, the method no longer reconstructs well. The simulation results are shown in Fig. S11. Secondly, our approach is based on a few-slit interference model, which will fail if the bandwidth is too large and the pulse duration is too short to span at least two temporal attosecond slits. The method works when the pulse duration is one optical cycle, but fails when the duration is reduced to 0.8 optical cycles. The simulation results are shown in Fig. S12 and Fig. S13.

Section 8: Simulation of the reconstruction with different wavelength of the perturbing field

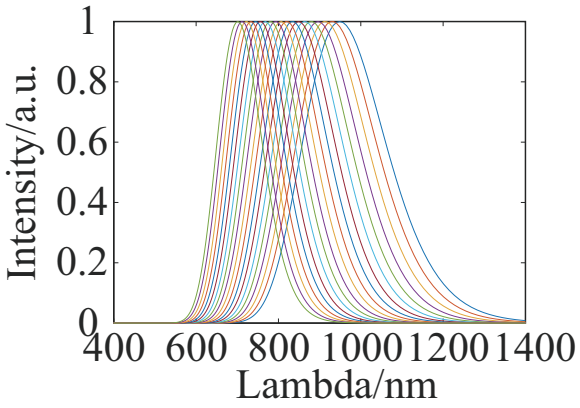

Figure S14: The spatial spectrum of the perturbing field with spatial chirp effect in the manuscript. Different colors represent different spatial locations.

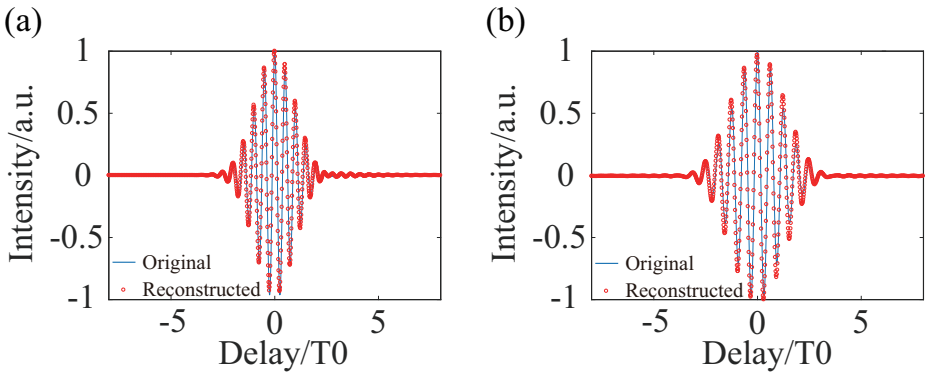

Figure S15: (a) and (b) The comparison of the reconstructed and original electric fields after introducing the perturbing field with 390 nm (500 nm) wavelength.

Our method is mainly limited by spectral bandwidth and intensity, but not by frequency of the perturbing field. Our simulation results show that the laser pulse can be reconstructed successfully (Figure 2 in the manuscript) even for a spectrum spanning from 600 to 1000 nm (Fig. S14). We also proved the reliability of our method for a second harmonic (390 nm, 3-cycle pulse duration) as well as a non-integer harmonic (500 nm, 3-cycle pulse duration) perturbing field, and the results are shown in Fig. S15.